LA-UR-21-23843
Approved for public release; distribution is unlimited.

Title: Dust Formation and Growth in Supernovae Explosions

Author(s): Stangl, Sarah Marie

Intended for: Doctoral General Exam Background Paper
Report

Issued: 2021-04-20

Disclaimer:
Los Alamos National Laboratory, an affirmative action/equal opportunity employer, is operated by Triad National Security, LLC for the National Nuclear Security Administration of U.S. Department of Energy under contract 89233218CNA000001. By approving this article, the publisher recognizes that the U.S. Government retains nonexclusive, royalty-free license to publish or reproduce the published form of this contribution, or to allow others to do so, for U.S. Government purposes. Los Alamos National Laboratory requests that the publisher identify this article as work performed under the auspices of the U.S. Department of Energy. Los Alamos National Laboratory strongly supports academic freedom and a researcher's right to publish; as an institution, however, the Laboratory does not endorse the viewpoint of a publication or guarantee its technical correctness.

Draft version April 9, 2021
Typeset using LaTeX **manuscript** style in AASTeX63

Dust Formation and Growth in Supernovae Explosions

Sarah M. Stangl[1,2]

[1] *University of Oklahoma, Norman, OK, 73019, USA*

[2] *Center for Theoretical Astrophysics, Los Alamos National Laboratory, Los Alamos, NM, 87545, USA*

(Accepted April 9, 2021)

ABSTRACT

Dust is a multi-messenger probe able to explore the dynamics of the Supernova Engine. The yield and composition of grains formed in the Supernova explosion are dependant on the initial explosion characteristics of the progenitor and on the explosion mechanism. Using dust as a probe, the dynamics of dust formation and growth is modeled in a diverse set of Core-Collapse Supernovae Explosions (CCSNe). The progenitor mass, explosion energy, engine type, and composition are varied across 72 models. The explosion is evolved using a 1-D Lagrangian Hydro-dynamical code (hydrocode) to roughly 3 years. A multi-grain nucleation and dust growth model is used to post process the hydrocode results and model grain formation and growth. The results show an earlier onset of grain formation, a larger silicate grain abundance, and smaller grain sizes in high explosion energy models.

1. INTRODUCTION & BACKGROUND

At the end of a massive star's life, a star greater than eight times the mass of the Sun, it undergoes a violent death. To maintain hydrostatic equilibrium in their cores, stars fuse heavier and heavier elements. Once iron fusion is reached, more energy is used to fuse iron than is released in the fusion

[1] The work presented here has been submitted to the Astrophysical Journal as Brooker et al. (2021)

process. Gravity overcomes the outward radiation pressure and collapse begins. The core collapses from about the size of the Earth down to about the size of Manhattan. A proto-neutron star (PSN) forms. Material in free fall towards the center compresses onto the core until nuclear matter density is reached. At this point, the core can no longer compress and material rebounds off, forming an outwards propagating shockwave. The shockwave loses energy and quickly stalls as it passes outwards about 100 km into the surrounding medium. At this time, neutrinos are able to escape the PSN, passing through and depositing energy in the stalled shock, reviving it. As the re-energized shockwave passes through density gradients, smaller reverse shocks are sent back towards the core. When the shock breaks through the stellar surface, it explodes into a core collapse supernova explosion (CCSN).

As the ejecta expands and cools, ionized plasma recombines into gaseous material. Gas-phase chemistry occurs, changing the initial composition of the gas (Sluder et al. 2018). Further cooling allows condensation out of the gas phase forming condensation nuclei in high density regions, dust grains. Surrounding gaseous material sticks to the surface of the nuclei in surface growth of the dust grains. Grains also grow from the colliding and sticking of smaller grains.

Dust grains interact with both the forward and reverse shocks. A shock increases the temperature and density as it passes through gas and dust. Dust is eroded and destroyed through thermal (dust moving with the shock) and non-thermal (the shock wave collides with stationary grains) sputtering (Biscaro & Cherchneff 2016). The collisions between ions and particles in the shock transfers kinetic energy to the grains. If the transferred energy is large enough to overcome surface bonds, surface material breaks off the grain (Nozawa et al. 2006). The eroded material is converted back into the gas phase and can form new grains or grow other grains. Shocks convert material back into the gas phase, but the shock also starts grain nucleation and growth by sweeping up material and increasing the local density.

Dust dynamics are simulated in a set of supernovae explosions covering a range of initial parameters. The produced dust is compared against the model parameters in order to use dust as a way to probe supernovae. Section 2 outlines the physics used in the supernovae and dust simulations, section 3 summarizes the results of the simulations, section 4 discusses future work and summarizes the results.

2. METHODS

To model dust formation and dust growth, the collapse, explosion, and evolution of the ejecta is simulated and run out to late times. The collapsed core is removed from the progenitor model. A stellar wind is mapped onto the outer regions and the model is re-meshed. Using a 1-Dimensional hydrodynamical code, the explosion is run out to about three years. The resulting temperature/density profiles are then post-processed to model dust grain formation and growth. These steps are described in more detail below.

2.1. *CCSNe Models*

A set of 1D CCSN models are taken from Fryer et al. (2018) and Andrews et al. (2020). A 1D Lagrangian hydrodynamical code (Herant et al. 1994; Fryer et al. 1999) is used to simulate the explosion by injecting energy mixed into a pre-determined convective region. It includes a gray flux-limited diffusion scheme with 3-neutrino flavors (electron, anti-electron, and μ plus τ neutrinos), equations of state to model nuclear densities, and an ideal gas equation of state for low densities. At high temperatures, $\sim$ T $> 5 \times 10^9$ K, a nuclear statistical equilibrium is assumed. A 17-isotope network is used at lower temperatures.

The progenitor masses and explosion properties are varied to produce seventy-two unique CCSNe models. These models have progenitor masses of 15, 20, and 25 $M_\odot$, explosion energies of $10^{51} - 10^{53}$ ergs, and varying nucleosynthetic isotopic yields. Table 2 summarizes the model properties. The energy injection methods include a sudden energy source to simulate a convective engine and a prolonged source such as a magnetar or fallback accretion. The explosion ejecta's velocity and composition depend on the progenitor's mass and explosion energy. Figure 1 shows the initial compositions of two 15, 20, and 25 $M_\odot$ progenitor models.

2.2. *Late-Time Evolution*

The compact object's core is removed and remeshed onto a grid extending out to 2.5×10^{19} cm. A constant velocity, constant entropy, stellar wind profile from Villata (1992) is stitched onto the stellar surface.

The wind follows,

$$\dot{M}_{\rm wind} = 1.2 \left(\frac{D^{\delta} \dot{M}_{\alpha}^{CAK}}{1+\alpha} \right)^{1/(\alpha-\delta)} \tag{1}$$

where D and $\dot{M}_{CAK}$ (Castor et al. 1975) are

$$\begin{aligned} D &= \left(\frac{1+Z_{He}Y_{He}}{1+4Y_{He}} \right) \left(\frac{9.5\times10^{-11}}{\pi m_H R_*^2 v_\infty} \right) \\ \dot{M}_{CAK} &= \frac{4\pi G M_* \alpha}{\sigma_E v_{th}} \left[k\Gamma \left(\frac{1-\alpha}{1-\Gamma} \right)^{1-\alpha} \right] \end{aligned} \tag{2}$$

where Z_{He} is the free electrons from helium, Y_{He} is the helium number abundance w.r.t. H, m_H is the mass of hydrogen ion, σ_E is Thomspon scattering absorption coefficient per mass density, $\Gamma = L/L_E$ is the ratio of stellar to Eddington luminosity, v_∞ is the escape velocity, v_{th} is thermal velocity, and k is a force multiplier. With a β velocity law

$$\begin{aligned} v(r) &= v_\infty \left(1 - \frac{r_0}{r} \right)^{\beta} \\ \beta &= 0.95\alpha + \frac{0.008}{\delta} + \frac{0.032 v_{esc}}{500} \end{aligned} \tag{3}$$

where v_{esc} is the escape velocity, in km s^{-1}. For the wind parameters k, α, δ, 0.17, 0.59, 0.09 are used.

The wind density is calculated assuming mass conservation using the mass loss rate ($\dot{M}_{CAK}$),

$$\rho_{\rm wind}(r) = \dot{M}_{CAK}/(4\pi r^2 v(r)) \tag{4}$$

When the wind density drops below the interstellar medium density of 2.09×10^{-24} g/cm^3, the density is set to the interstellar medium density.

The explosion from the CCSNe calculations and the wind density profiles are remapped onto a grid of 2048 Lagrangian zones. Then the explosion is carried out to late times ($\sim$ 3 years) using the CCSN code without neutrino transport or equations of state for dense matter.

Figure 2 shows the temperature, density, and velocity profiles for a 15 $M_\odot$, 1.69 foe (ten to the *F*ifty *O*ne *E*rgs) model at a range of times after the explosion. Shock waves are evident between $0.2-2M_\odot$ as a sudden drop in the profile. As the shock propagates into the wind medium, it decelerates and

creates reverse shocks as seen in the velocity profiles at different times. The effects of shock waves on dust grains is not currently modeled in the dust code, but it contains the relevant information and will be studied in the future. The heating caused by the shocks on the surrounding material is included in the dust code.

The calculations provide temperature and density profiles as a function of time for each cell. Figure 2 shows the density and temperature evolution for the zones in the 15 $M_\odot$ 1.69 foe model. The abundances from the CCSNe calculations and the temperature-density profiles needed for dust formation calculations.

2.3. *Dust Formation*

As the ejects expands and cools, it reaches conditions where the gas-phase pressure-temperature state is thermodynamically metastable and a phase transition is energetically favorable. A kinetic energy barrier prevents the phase transition. This is overcome by nucleation. Molecules in the new phase grow by Boltzmannic attachment, eventually leading to spontaneous growth through the formation of stable critical clusters.

The formation of molecules decreases the free-energy, but an excess free-energy is needed to maintain surface tension. A modified version of Classical Nucleation Theory, simplifying molecular clusters as nano-particles of the bulk stable phase, utilizing key species is followed (Nozawa & Kozasa 2013). A key species is the gaseous reactant with the lowest collision frequency and has a reaction rate larger than its decay rate (Kozasa & Hasegawa 1987). The key species and reactions used to model each dust grain is shown in Table 1.

The kinetics of nucleation rate and grain growth is governed by the key species. The steady state nucleation rate, $J_j^s(t)$ for the jth species is given by,

$$J_j^s(t) = \alpha_{sj}\Omega_j \left(\frac{2\sigma_j}{\pi m_{1j}}\right)^{1/2} \left(\frac{T}{T_d}\right)^{1/2} \Pi_j c_{1j} e^{-4\mu_j^3/27(lnS_j)^2}. \tag{5}$$

α_{sj} is the sticking probability of the key species (KS) and is assumed to be 1, Ω_j is the volume of condensate per molecule of the KS, σ_j is the surface energy, c_{1j} is the concentration of KS, m_{1j}

is the mass of KS, T_d is the temperature of the condensation nuclei, T is the gas temperature, Π_j is a function of gas pressures and is set to 1, μ_j is the energy barrier for nucleation, and S_j is the supersaturation ratio.

In supernovae ejects, the timescale for cooling, growth, and nucleation are similar to the dynamical timescale. A non-steady state nucleation rate is used,

$$\frac{\partial}{\partial t}\frac{J_j(t)}{\eta_j} = -\frac{1}{\tau_{*j}\eta_j}[J_j(t) - J_j^s(t)] \tag{6}$$

with the relaxation time,

$$\tau_{*j}^{-1} = \tau_{coll,j}^{-1}\frac{(lnS_j)^2}{\mu_j} \tag{7}$$

where $\tau_{coll,j}$ is the collision time of KS and η_j is a function of collision time and the critical grain radius, $r_{c,j}$.

The grain growth is given by,

$$\frac{dr_j}{dt} = \alpha_{sj}\Omega_j\left(\frac{kT}{2\pi m_{1j}}\right)^{1/2} c_{1j}(t) = \frac{1}{3}a_{0j}\tau_{coll,j}^{-1}(t) \tag{8}$$

where k is the Boltzmann constant.

The abundance of each key species drives the growth and nucleation. Once a key species is used up, the reactions stop and no new grains form or grow for the dependant grain species. The abundance of the key species is determined by a system of coupled ODEs. Integrating the equation of continuity for the key species produces,

$$\frac{dK_j^{(i)}}{dt} = \frac{J_j(t)}{\tilde{c}_{1j}(t)}\frac{4\pi}{3\Omega_j}r_{c,j}^i + iK_j^{(i-1)}\frac{dr_j}{dt} \tag{9}$$

where $\tilde{c}_{1j}(t)$ is the nominal concentration of the KS without depletion. Equation 9 describes the three moments for $i = 1, 2, 3$ and

$$\frac{dK_j^0}{dt} = \frac{J_j(t)}{\bar{c}_{1j}(t)}\frac{4\pi}{3\Omega_j}. \tag{10}$$

Equations 9 and 10 are solved simultaneously for each grain species at each time step. These moments give the number density $n_{gr,j}(t)$ and the average radius $r_{gf,j}(t)$ of each grain at that time step,

$$\frac{n_{gr,j}}{\tilde{c}_{1j}} = a_0^3 K^(0)_j(t) \tag{11}$$

and

$$r_{gr,j}^3 = \frac{K_j^{(3)}(t)}{K_j^{(0)}(t)}. \tag{12}$$

The size distribution of the grains is given by,

$$f_j(r)dr = a_{0j}^3 \tilde{c}_{1j} \frac{dK_j^{(0)}(t')}{dt'} dt' \tag{13}$$

2.4. *Code*

The dust kinetics are implemented in a python code *nuDust*[1]. It uses NumPy (Harris et al. 2020) and SciPy (Virtanen et al. 2020) for numerical methods and integrations. The library numba (Lam et al. 2015) is used for just-in-time (JIT) compilation of python code to increase efficiency and optimize parallelization. It takes in the grain reaction networks, the initial model composition, and the temperature-density hydrocode results.

Before integration begins, the temperature and density values are interpolated in time using a cubic piece-wise polynomial spline (Akima 1970). All available carbon, oxygen, and silicon is formed into CO and SiO molecules. The temperature, density, and their derivatives are calculated at the beginning of each time step. The system of coupled ODEs is solved simultaneously for each grain species until all they key species are exhausted or the temperature falls below the threshold for nucleation and grain growth. SciPy's LSODA (Hindmarsh 1983) integrator is used to solve the ODEs.

[1] https://github.com/lanl/sndust

3. RESULTS

A large database of varying CCSNe models is acquired by continuing the hydrodynamical calculations of models taken from Fryer et al. (2018) out to 1157 days. These include progenitor masses of 15, 20, 25, $M_\odot$, explosion energies between $0.3-124$ foe, and varied initial abundance compositions.

The temperature and density profiles from these calculations are needed as input for the dust formation code. The dust code was also run out to 1157 days to allow dust formation to complete. The equations discussed in Section 2 are used to calculate the dust mass and average energy as function of time. Table 3 shows the dust mass per grain species produced in each model.

3.1. *Distribution of Grains in Ejecta*

A comparison of the dust fraction (top panel) and gas fraction (bottom panel) versus location site within the progenitor for dust formation is shown in Figure 3 (15 $M_\odot$), 4 (20 $M_\odot$), and 5 (25 $M_\odot$). Figure 3 shows the distribution for a 15 $M_\odot$, 3.42 for model, Figure 4 a 20 $M_\odot$, 2.60 for model, and Figure 5 a 25 $M_\odot$, 4.73 foe model.

All three models have similar distributions of grain formation. In the outer region of the ejecta, the hydrogen envelope, a small amount of high metallicity material is available leading to a smaller fraction of grain mass. The helium envelope produces a small amount of Si and C dust grains in the 15 $M_\odot$ progenitor, but larger amounts in the 20 and 25 $M_\odot$ progenitors. The carbon layer is the site of a large amount of carbon dust. The overlap between the carbon and oxygen layers produce a region high in CO gas, ending carbon dust formation. At the CO/Si interface, carbon locks up the available oxygen in CO gas until carbon is depleted. Then SiO forms leading to the prevalence of $MgSiO_3$ and small amounts of Al_2O_3 and Mg_2SiO_4 in this region. Moving on into the oxygen layer, a relatively large amount of oxide dust is formed: Mg_2SiO_3, Al_2O_3, Mg_2SiO_4, and SiO_2.

3.2. *Grain Sizes*

The average grain mass as a function of time per species is shown in Figure 7. Carbon grains form earlier and produce smaller grains in higher energy explosions. The fast evolution of the ejecta, fast expansion, and fast cooling leave a smaller window of time where the conditions are conducive

for grain formation and growth and the ejecta cools quicker allowing for an earlier onset of dust formation. All models produce grains with an average size of $\sim 10^8 - 10^{-7}$ cm. In general, the lower explosion energy models produced larger grains. This is attributed to the slower evolution of the ejecta and despite grains nucleating later, the ejecta takes longer to cool and expand to temperatures and densities where dust growth cannot occur. Low explosion energy models evolve slower and dust grains are able to grow and nucleate for longer periods of time.

3.3. *Grain Mass*

Figure 6 and 8 show the dust mass as a function of time. Bulk formation (nucleation) of grains occurs at earlier times in higher explosion energy models and is seen as vertical jumps in Figure 6. Bulk formation occurs first for carbon grains followed by aluminum oxide (Al_2O_3), fosterite (MgO_3), and enstatite (Mg_2SiO_4).

The left panel of Figure 8 shows the amount of total dust produced as a function of time with the colors indicating the explosion energy. In the 15 and 20 $M_\odot$ models, higher explosion energies produced earlier formation of dust. They also produce a larger amount of total dust. In the 25 $M_\odot$ case, a clear trend is not readily apparent. The speed of the innermost ejecta depends on the supernova engine (sudden versus prolonged explosion) and leads to this lack of uniformity.

The right panel of figure 8 shows the production time of silicate (dashed lines) and carbon (solid lines) grains. Colors again represent the explosion energy of the models. Carbon grains form earlier than silicate grains in the 15 and 20 $M_\odot$ models. The silicate layer of the ejecta is located deeper in the star than the carbon layer and so it takes longer for it to expand and cool to temperatures and densities conducive for silicate dust formation. The variation in the engines in the 25 $M_\odot$ creates a weaker trend between the order of dust formation.

Figure 9 shows the mass ratio of carbon, silicate, oxide, sulfide, and iron dust to total dust produced after dust formation ceases at $\sim\ 3 - 15$ years. Across all progenitor masses the most commonly produced dust grains are silicates. However at certain explosion energies for the 15 $M_\odot$ (1-2 foe) and 20 $M_\odot$ ($\sim$ 15-80 foe) models there are more carbon grains produced than compared at higher explosion energies (see Figure 9 top and middle panels). One explanation for the drop off of carbon

dust is carbon burning. With an energetic enough explosion, carbon is burned into material that is necessary for silicate growth leading to an increase in silicate dust and a decrease in carbon dust. At high explosion energies and as the energy is increased, the amount of carbon dust produced remains nearly constant. This is most apparent in the 15 and 25 $M_\odot$ cases. In Figure 8, the solid carbide lines in the right panel for high explosion energies are grouped together, meaning similar amounts of carbide dust.

4. FUTURE WORK

4.1. *nuDUST*

Currently, nuDust models the formation and growth of dust grains through nucleation of material out of the gas phase and incoming ions sticking to the grains. Future goals involve including more realistic physics. Grain erosion and destruction occurs when the surrounding media collides and interacts with the grains. Grains also stick together through accretion as a source of growth. This allows for a more comprehensive analysis of total dust production and size before injection into the ISM.

4.2. *Models*

More realistic phsyics will be added to the models. Currently, the models have a constant entropy stellar wind. In the future, more realistic winds will be added along with density fluctuations representing previously ejected material from stellar outbursts. Additionally, the models do not include any mixing of the stellar material. This isn't physical and could be responsible for some results (bulk carbon grains form before silicates while it is generally believed the opposite is true). Mixing will be included in the future.

4.3. *PHOENIX*

PHOENIX is a radiative transfer code used to model general atmospheres and produce the corresponding spectra. In particular, it is useful in modeling turbulent atmospheres such as Supernovae. Future work includes implementing molecules, grain cross sections, and abundances in PHOENIX by

potentially including Mie scattering effects. Then using this scheme to produce early and late time spectra from the seventy-two 1D CCSN models. These synthetic spectra can then be compared with observations to look at the effect of different explosion energies, abundances, progenitor masses, etc. on the resulting CCSN spectra.

5. CONCLUSIONS

A set of 72 supernovae explosions with varying explosion energies, progenitor masses, and composition were run out to late times. A 1-D Lagrangian hydrocode was used to model the evolution of the ejecta. The resulting explosion temperature density profiles were used as inputs into a post processing dust code to simulate dust grain formation and growth.

This suite of supernovae progenitors is used to study the dependence of dust production on the properties of the supernova explosion. Higher explosion energy models produce an earlier onset of dust formation. This is due to the faster expansion and cooling of the ejecta. The average dust grain is smaller than those produced in the low energy models. Again this is attributed to the faster expansion and cooling. High energy explosions quickly evolve to conditions amenable to dust formation but also quickly become too cold and too sparse for dust formation. This results in a shorter growth stage and smaller grains.

The stellar material in these models is unmixed and includes simple stellar winds. Future work will be done to include more accurate physics, including mixing and more realistic stellar winds, in order to form a more comprehensive study of how dust formation depends on the properties of the supernova explosion.

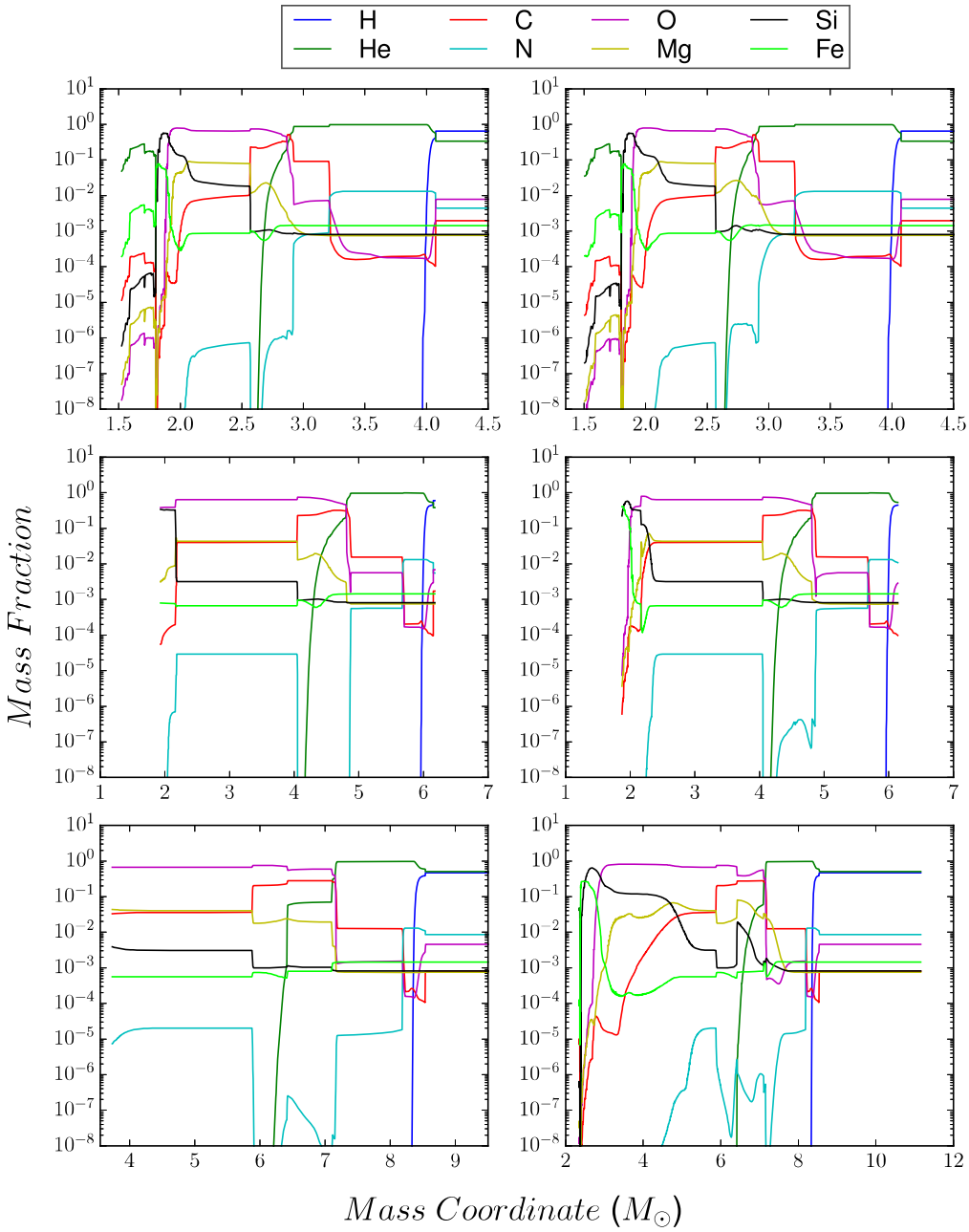

Figure 1. Plotted above are the abundance profiles for eight elements important in grain formation. Top: the top row has two 15 $M_\odot$ progenitor models (L: 1.69 foe, R: 3.43 foe). Middle: two 20 $M_\odot$ progenitors (L: 1.39 foe, R: 5.9 foe). Bottom: two 25 $M_\odot$ progenitors (L: 1.57 foe, R: 14.8 foe). Models of the same progenitor mass have similar abundance profiles. As the explosion energy is varied, the distribution profile of Nitrogen, Magnesium, and Silicon change the most. Increasing the explosion energy while keeping the progenitor mass constant, the structure of the material becomes less uniform as seen in the $25M_\odot$ models. Figure taken from Brooker et al. (2021)

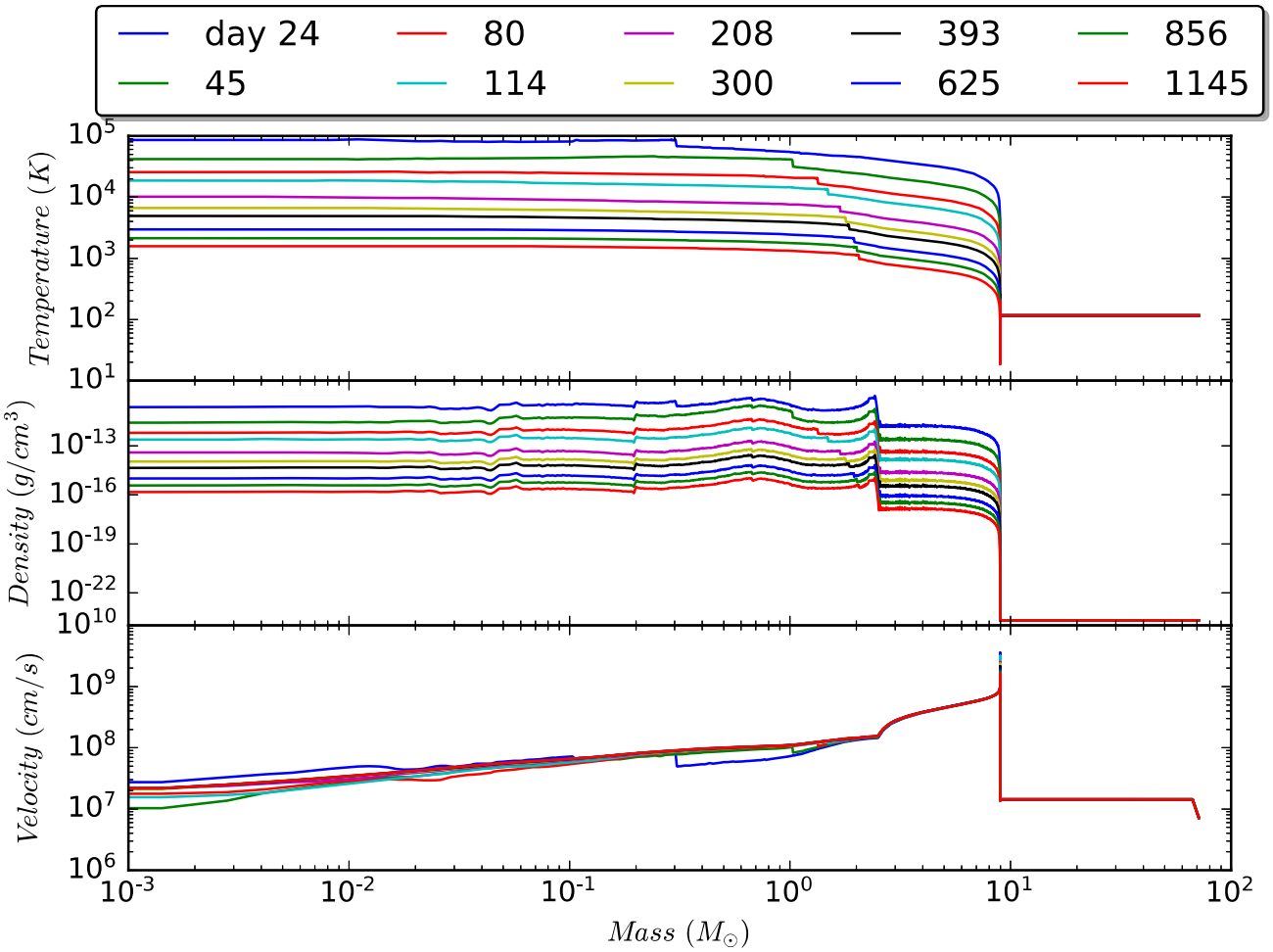

Figure 2. Plots of they hydrodynamical profiles for a 15 $M_\odot$, 1.69 foe progenitor model at 10 different timesteps. Top: the temperature profile as a function of mass coordinate, Middle: density versus mass coordinate, Bottom: velocity versus mass coordinate. The horizontal lines to the right of 10 $M_\odot$ are due to the stitched on stellar wind. Outwards propagating shocks can be seen between 1-2 $M_\odot$ as steep decreases in the respective profiles. Figure taken from Brooker et al. (2021)

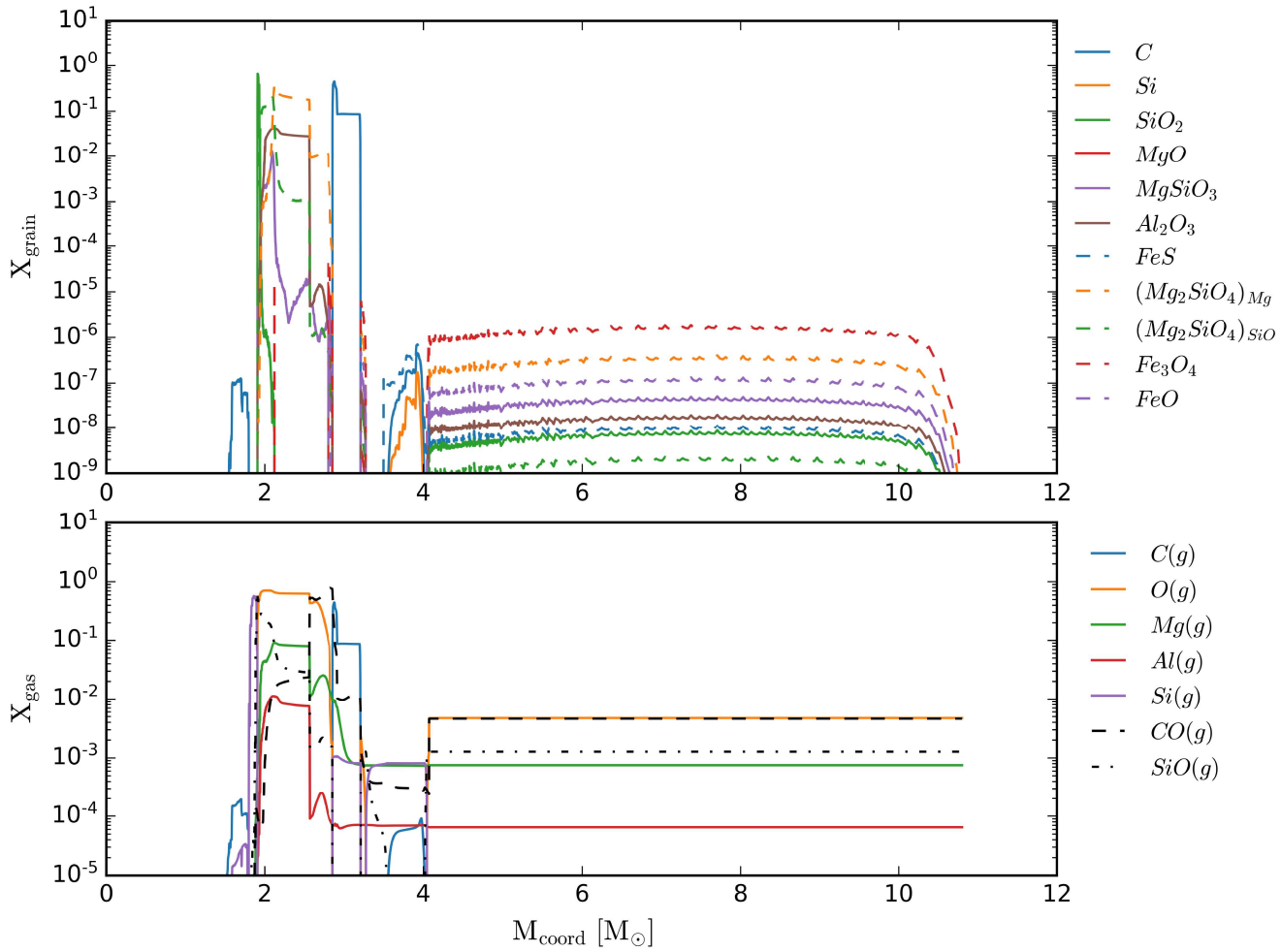

Figure 3. Gas and dust distribution for a 15 $M_\odot$ 3.42 foe model. Bottom: distribution of gas phase elements and molecules mass versus mass coordinate. Figure taken from Brooker et al. (2021)

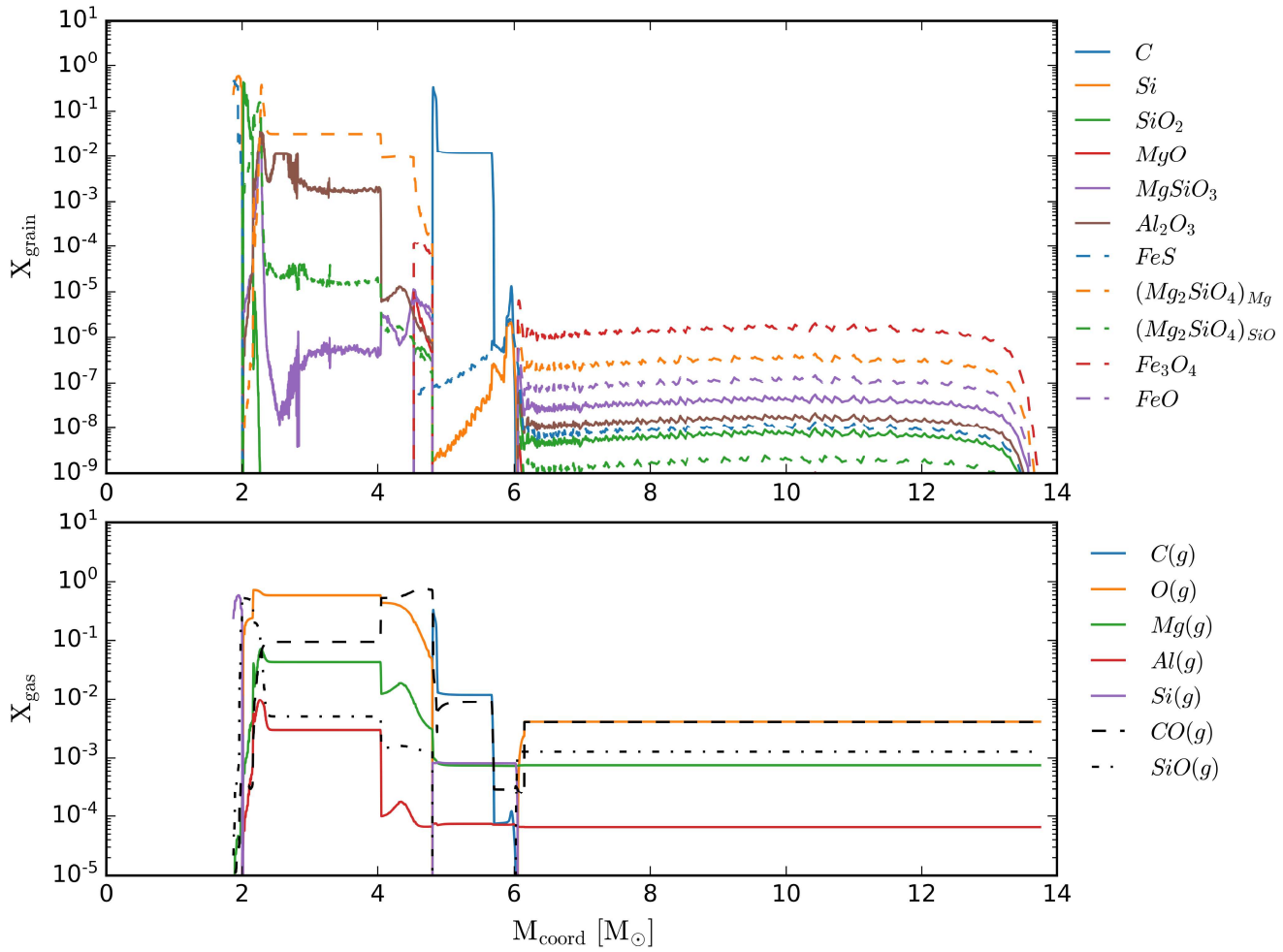

Figure 4. Gas and dust distribution for a 20 $M_\odot$ 2.60 foe model. Top: profile of dust grain mass as a function of mass coordinate. Bottom: distribution of gas phase elements and molecules mass versus mass coordinate. Figure taken from Brooker et al. (2021)

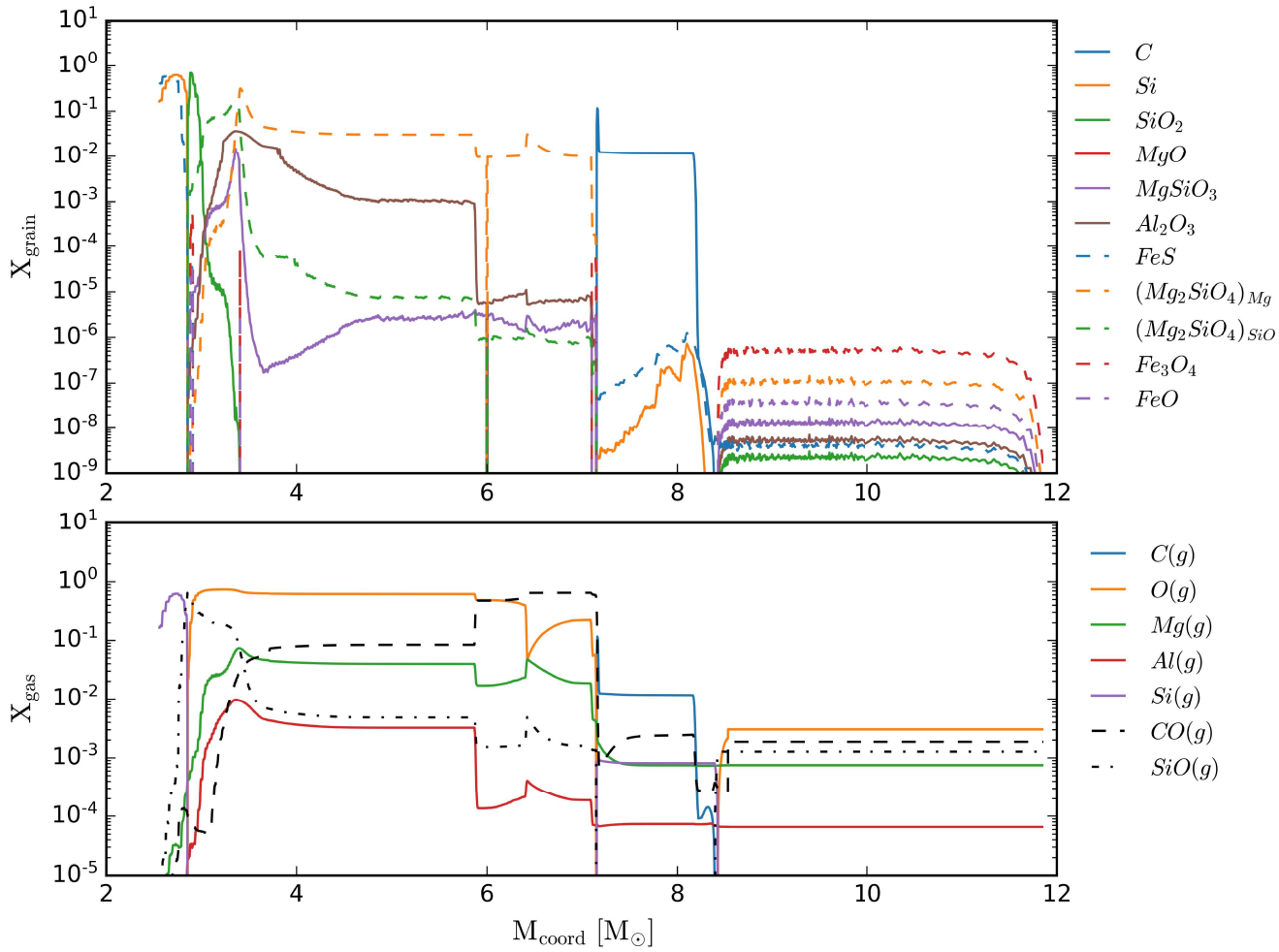

Figure 5. Gas and dust distribution for a 25 $M_\odot$ 4.73 foe model. Bottom: distribution of gas phase elements and molecules mass versus mass coordinate. Figure taken from Brooker et al. (2021)

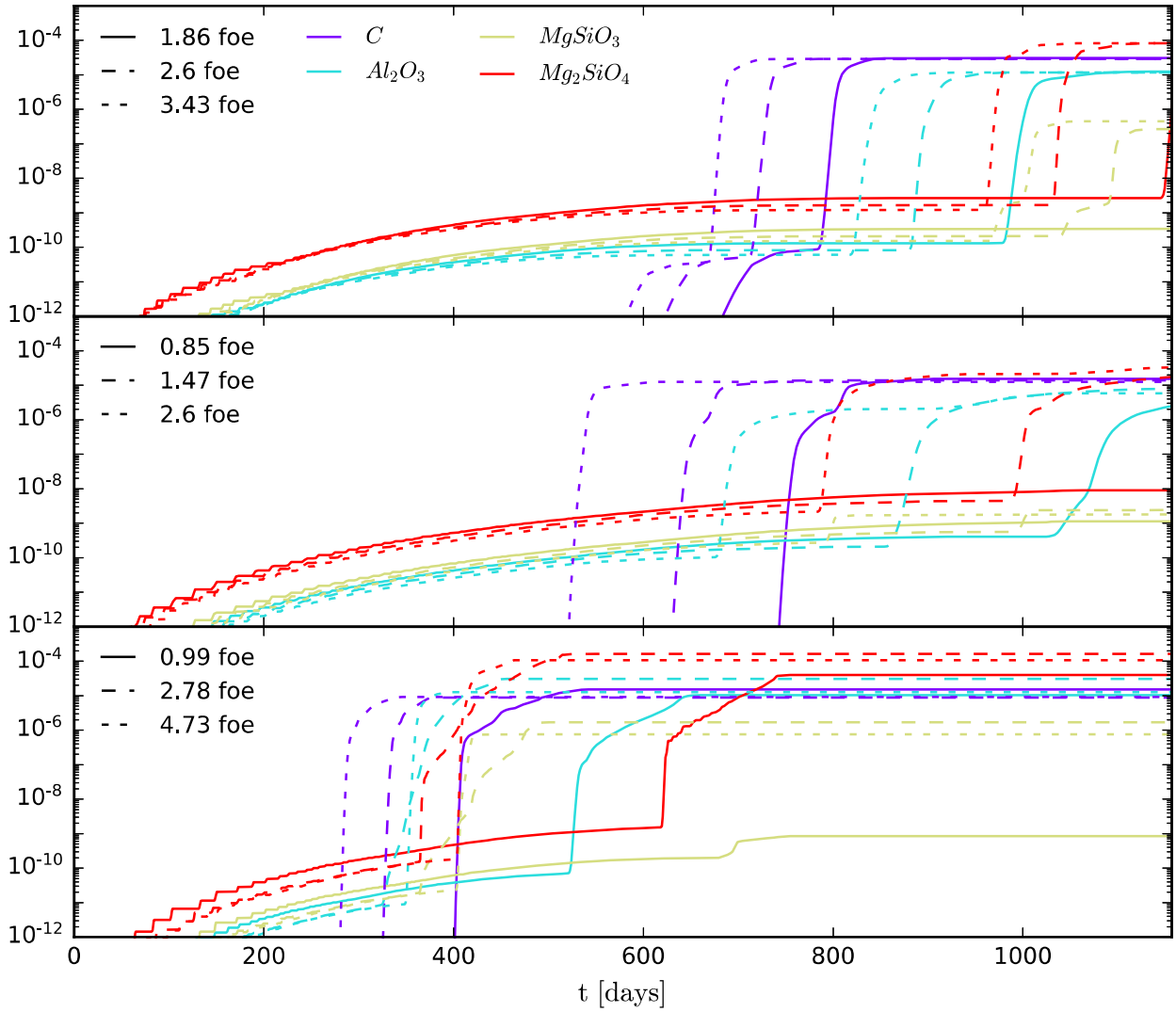

Figure 6. The total dust mass per species is plotted as a function of time. Top: 15 $M_\odot$ models with explosion energies of 1.86, 2.60, and 3.43 foe. Middle: 20 $M_\odot$ models with explosion energies of 0.85, 1.47, and 2.60 foe. Bottom: 25 $M_\odot$ models with explosion energies of 0.99, 2.78, and 4.73 foe. Figure taken from Brooker et al. (2021)

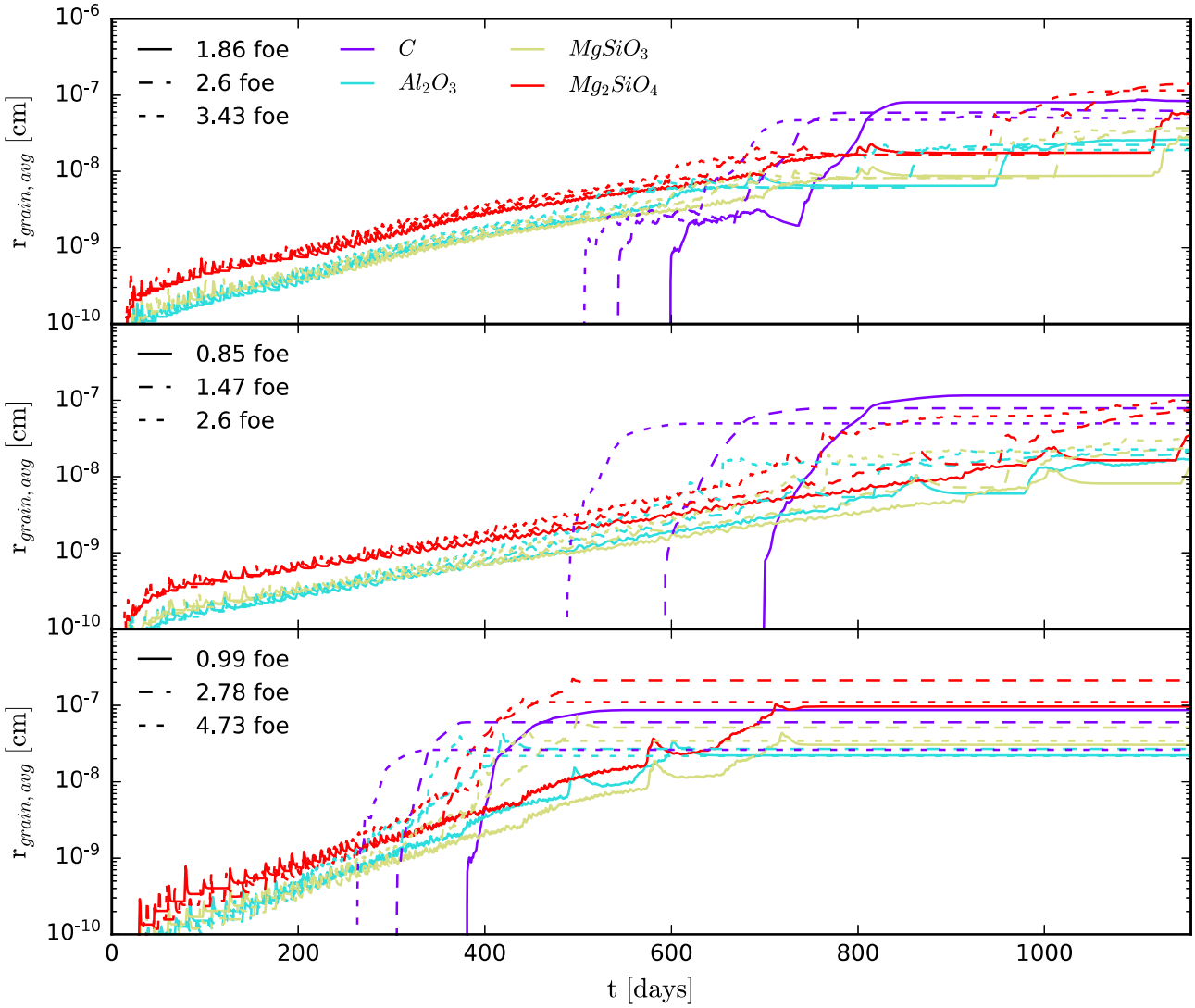

Figure 7. The average grain radius per species is plotted as a function of time. Top: 15 $M_\odot$ models with explosion energies of 1.86, 2.60, and 3.43 foe. Middle: 20 $M_\odot$ models with explosion energies of 0.85, 1.47, and 2.60 foe. Bottom: 25 $M_\odot$ models with explosion energies of 0.99, 2.78, and 4.73 foe. Figure taken from Brooker et al. (2021)

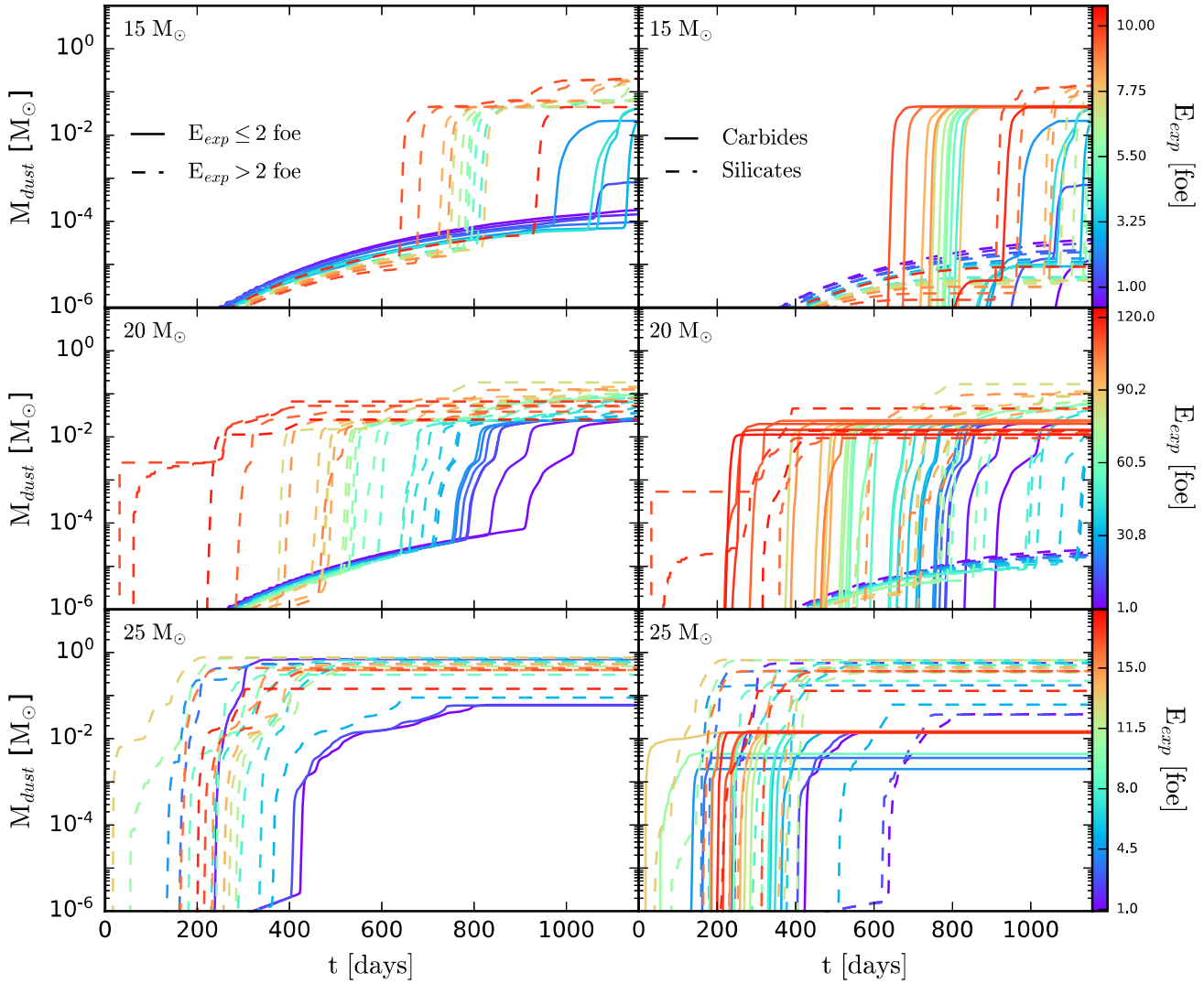

Figure 8. Left Column: the total dust mass plotted as a function of time. Different colors correspond to different explosion energies. Dashed lines represent explosion energies $\leq$ 2 foe and solid lines represent explosion energies 2 foe. Right Column: the total dust mass for carbides (solid line) and silicates (dashed lines) as a function of time. Top: 15 $M_\odot$ progenitor models. Middle: 20 $M_\odot$ progenitors. Bottom: 25 $M_\odot$ models. Figure taken from Brooker et al. (2021)

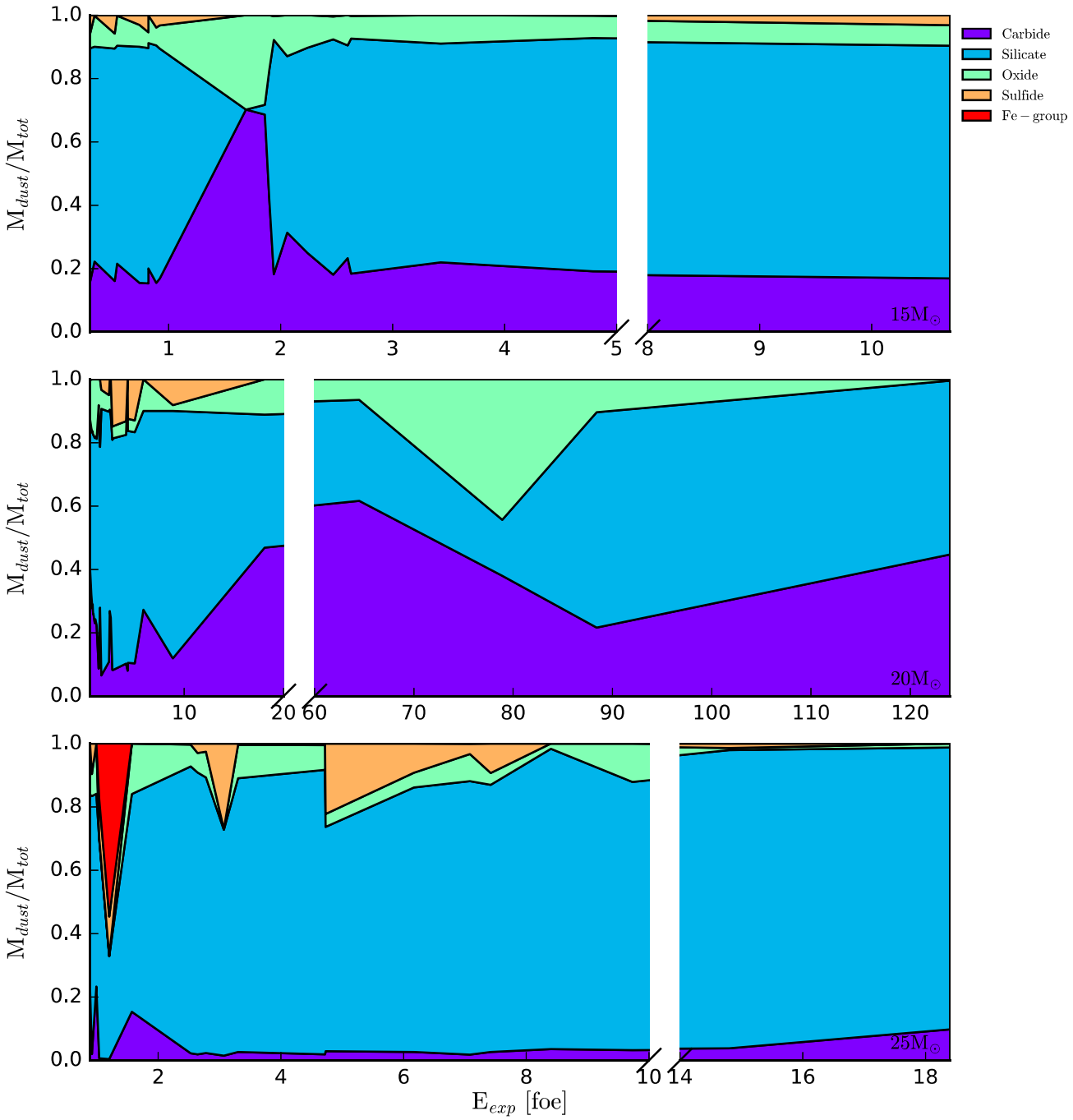

Figure 9. Continuous stacked 'bar plots' representing the ratio of each grain mass to the total mass produced after dust stops forming ($\sim$ 3 − 15 years) as a function of explosion energy. Top: 15 $M_\odot$ progenitor models. Middle: 20 $M_\odot$ progenitors. Bottom: 25 $M_\odot$ models. Figure taken from Brooker et al. (2021)

Table 1. Dust grain reaction table taken from Nozawa et al. (2003).

Grain	Key Species	Formula	A/10^4(K)	B	σ(erg/Å^2)	a_0(Å)
(1)	(2)	(3)	(4)	(5)	(6)	(7)
C	C(g)	C(g) $\rightarrow$ C	8.64726	19.0422	1400.0	1.281
SiC	Si(g), C(g)	Si(g) + C(g) $\rightarrow$ SiC	14.8934	37.3825	1800.0	1.702
TiC	Ti(g), C(g)	Ti(g) + C(g) $\rightarrow$ TiC	16.4696	37.2301	1242.0	1.689
Si	Si(g)	Si(g) $\rightarrow$ Si	5.36975	17.4349	800.0	1.684
$MgSiO_3$(s)	Mg(g), SiO(g)	Mg(g) + SiO(g) + 2O(g) $\rightarrow$ $MgSiO_3$(s)	25.0129	72.0015	400.0	2.319
Mg_2SiO_4(s)	Mg(g)	2Mg(g) + SiO(g) + 3O(g) $\rightarrow$ Mg_2SiO_4(s)	18.6200	52.4336	436.0	2.055
Mg_2SiO_4(s)	SiO(g)	2Mg(g) + SiO(g) + 3O(g) $\rightarrow$ Mg_2SiO_4(s)	37.2400	104.872	436.0	2.589
SiO_2(s)	SiO(g)	SiO(g) + O(g) $\rightarrow$ SiO_2(s)	12.6028	38.1507	605.0	2.080
Al_2O_3(s)	Al(g)	2Al(g) + 3O(g) $\rightarrow$ Al_2O_3(s)	18.4788	45.3543	690.0	1.718
MgO(s)	Mg(g)	Mg(g) + O(g) $\rightarrow$ MgO(s)	11.9237	33.1593	1100.0	1.646
FeO(s)	Fe(g)	Fe(g) + O(g) $\rightarrow$ FeO(s)	11.1290	31.9850	580.0	1.682
Fe_3O_4(s)	Fe(g)	3Fe(g) + 4O(g) $\rightarrow$ Fe_3O_4(s)	13.2889	39.1687	400.0	1.805
FeS(s)	Fe(g), S(g)	Fe(g) + S(g) $\rightarrow$ FeS(s)	9.31326	30.7771	380.0	1.932
Ti(s)	Ti(g)	Ti(g) $\rightarrow$ Ti(s)	5.58902	16.6071	1510.0	1.615
V(s)	V(g)	V(g) $\rightarrow$ V(s)	6.15394	17.8702	1697.0	1.490
Cr(s)	Cr(g)	Cr(g) $\rightarrow$ Cr(s)	4.67733	16.7596	1880.0	1.421
Co(s)	Co(g)	Co(g) $\rightarrow$ Co(s)	5.03880	16.8372	1936.0	1.383
Fe(s)	Fe(g)	Fe(g) $\rightarrow$ Fe(s)	4.84180	16.5566	1800.0	1.411
Ni(s)	Ni(g)	Ni(g) $\rightarrow$ Ni(s)	5.09310	17.1559	1924.0	1.377
Cu(s)	Cu(g)	Cu(g) $\rightarrow$ Cu(s)	3.97955	14.9083	1300.0	1.412

Note—List of grain reactions. The parameters A, B are parameters for finding free energy[a] $-\Delta G/kT = -A/T + B$ σ gives experimentally determined surface tensions, and $a0$ is the expected monomer size.

[a]These values can be found using the NASA coefficients for individual species McBride (1993). In brief, $\Delta G = \Delta H - T\Delta S$. The polynomials given in McBride (1993) provide $\Delta H, \Delta S$ for the species to determine ΔG. Values presented here are fit to a simpler form $-A/T + B$, although this is not required.

Table 2. List of models used from Fryer et al. (2018).

Model	M_{prog}	M_{bounce}	M_{inj}	t_{inj}	E_{inj}	E_{exp}	M_{rem}
	($M_\odot$)	($M_\odot$)	($M_\odot$)	(s)	10^{51} erg	10^{51} erg	($M_\odot$)
(1)	(2)	(3)	(4)	(5)	(6)	(7)	(8)
M15aE0.34	15	1.30	0.3	0.1	3	0.34	1.94
M15aE0.54	15	1.30	0.3	0.1	4	0.54	1.91
M15aE0.82	15	1.30	0.3	0.1	5	0.82	1.88
M15aE2.47	15	1.30	0.3	0.1	9	2.47	1.52
M15aE4.79	15	1.30	0.3	0.4	20	4.79	1.50
M15bE0.30	15	1.30	0.02	0.4	3	0.3	1.71
M15bE0.52	15	1.30	0.02	0.2	5	0.52	1.71
M15bE0.74	15	1.30	0.02	0.4	3	0.74	1.73
M15bE0.82	15	1.30	0.02	0.2	6	0.82	1.71
M15bE0.89	15	1.30	0.02	0.2	5	0.89	1.74
M15bE0.92	15	1.30	0.02	0.3	4	0.92	1.75
M15bE1.69	15	1.30	0.02	0.2	10	1.69	1.52
M15bE2.63	15	1.30	0.02	0.2	20	2.63	1.53
M15bE10.7	15	1.30	0.02	0.2	80	10.7	1.53
M15cE2.06	15	1.30	0.1	0.3	15	2.06	1.59
M15cE1.94	15	1.30	0.1	0.3	12	1.94	1.61
M15cE1.90	15	1.30	0.1	0.3	10	1.90	1.62
M15cE1.86	15	1.30	0.1	0.3	9	1.86	1.63
M15cE2.24	15	1.30	0.1	0.3	25	2.24	1.56
M15cE2.60	15	1.30	0.1	0.3	45	2.60	1.52
M15cE3.43	15	1.30	0.1	0.3	90	3.43	1.51
M20aE0.53	20	1.56	0.1	0.50	4	0.53	3.40
M20aE0.65	20	1.56	0.1	0.12	4	0.65	3.03
M20aE0.81	20	1.56	0.1	0.12	7	0.81	2.70
M20aE0.85	20	1.56	0.1	0.50	7	0.85	2.62
M20aE1.39	20	1.56	0.1	0.12	10	1.39	1.93
M20aE1.47	20	1.56	0.1	0.50	10	1.47	2.23
M20aE2.43	20	1.56	0.1	0.12	20	2.43	1.86
M20aE2.50	20	1.56	0.1	0.50	20	2.50	1.93
M20aE4.15	20	1.56	0.1	0.12	50	4.15	1.85
M20bE0.78	20	1.56	0.2	0.12	5	0.78	2.85
M20bE1.04	20	1.56	0.2	0.12	6	1.04	2.47
M20bE1.19	20	1.56	0.2	0.12	8	1.19	2.28
M20bE1.52	20	1.56	0.2	0.12	10	1.52	1.97
M20bE2.60	20	1.56	0.2	0.12	25	2.60	1.90
M20bE4.33	20	1.56	0.2	0.12	50	4.33	1.87
M20cE0.75	20	1.47	0.1	0.5	6	0.75	2.76

Table 2 *continued on next page*

Table 2 *(continued)*

Model	M_{prog}	M_{bounce}	M_{inj}	t_{inj}	E_{inj}	E_{exp}	M_{rem}
	($M_\odot$)	($M_\odot$)	($M_\odot$)	(s)	10^{51} erg	10^{51} erg	($M_\odot$)
(1)	(2)	(3)	(4)	(5)	(6)	(7)	(8)
M20cE0.84	20	1.47	0.1	0.5	7	0.84	2.62
M20cE1.00	20	1.47	0.1	0.5	8	1.00	2.35
M20cE1.65	20	1.47	0.1	0.5	10	1.65	1.78
M20cE2.76	20	1.47	0.1	0.5	15	2.76	1.76
M20cE2.85	20	1.47	0.1	0.5	20	2.85	1.74
M20cE5.03	20	1.47	0.1	0.5	50	5.03	1.74
M20cE8.86	20	1.47	0.1	0.5	100	8.86	1.74
M20dE4.33	20	1.56	0.2	0.12	50	4.33	1.87
M20dE5.90	20	1.47	0.2	0.5	20	5.9	1.74
M20dE18.1	20	1.47	0.2	0.5	50	18.1	1.74
M20dE64.5	20	1.47	0.2	0.5	75	64.5	1.74
M20dE78.9	20	1.47	0.2	0.5	100	78.9	1.74
M20dE88.4	20	1.47	0.2	0.5	125	88.4	1.74
M20dE124	20	1.47	0.2	0.5	150	124	1.74
M25aE0.99	25	1.83	0.1	0.1	5.0	0.99	4.89
M25aE1.57	25	1.83	0.1	0.1	10	1.57	3.73
M25aE4.73	25	1.83	0.1	0.1	20	4.73	2.38
M25aE6.17	25	1.83	0.1	0.1	35	6.17	2.38
M25aE7.42	25	1.83	0.1	0.1	50	7.42	2.37
M25aE14.8	25	1.83	0.1	0.1	100	14.8	2.35
M25bE8.40	25	1.83	0.02	0.28	50.0	8.40	2.38
M25bE9.73	25	1.83	0.02	0.69	100	9.73	2.35
M25bE18.4	25	1.83	0.02	0.69	200	18.4	2.35
M25d3E0.89	25	1.83	0.02	0.7	7	0.89	4.66
M25d3E0.92	25	1.83	0.02	0.7	8	0.92	1.84
M25d3E1.04	25	1.83	0.02	0.7	10	1.04	1.84
M25d3E1.20	25	1.83	0.02	0.7	50	1.20	1.84
M25d2E2.53	25	1.83	0.02	0.7	20	2.53	2.35
M25d2E2.64	25	1.83	0.02	0.7	35	2.64	2.35
M25d2E2.78	25	1.83	0.02	0.7	50	2.78	2.35
M25d2E3.07	25	1.83	0.02	0.7	100	3.07	1.83
M25d1E3.30	25	1.83	0.02	0.7	25	3.30	2.35
M25d1E4.72	25	1.83	0.02	0.7	50	4.72	2.35
M25d1E7.08	25	1.83	0.02	0.7	100	7.08	2.35

Note—List of supernova models used organized by progenitor mass denoted by uppercase "M" with progenitor mass in the model name. For each progenitor mass, lowercase alphabetic characters denote supernova engine subgroups. Subgroups are order by increasing explosion energy denoted with uppercase "E" and the explosion energy in the model name. Table columns: 1) Model, 2) Progenitor mass, M_{prog}, 3) Shock rebound mass, M_{bounce}, 4) Injection mass, M_{inj}, 5) Injection time, t_{inj}, 6) Injection energy, E_{inj}, 7) Final explosion energy, E_{exp}, 8) Mass of remnant, M_{rem}.

Table 3. Dust mass for specific species and total dust mass produced per model by 1157 days after explosion. Table taken from Brooker et al (2021).

Dust Species	Models							
	M15aE0.34	M15aE0.54	M15aE0.82	M15aE2.47	M15aE4.79	M15bE0.3	M15bE0.52	M15bE0.74
C	1.19×10^{-15}	6.96×10^{-7}	2.26×10^{-2}	4.47×10^{-2}	4.64×10^{-2}	1.27×10^{-5}	6.98×10^{-4}	2.14×10^{-2}
SiC	6.98×10^{-34}	6.17×10^{-15}	1.11×10^{-12}	2.67×10^{-12}	2.26×10^{-10}	7.34×10^{-14}	2.20×10^{-12}	3.45×10^{-12}
TiC	0	4.01×10^{-30}	1.47×10^{-12}	3.83×10^{-12}	7.53×10^{-13}	0	5.26×10^{-15}	9.95×10^{-13}
Si	0	0	0	2.77×10^{-10}	2.26×10^{-8}	0	0	0
SiO_2	5.86×10^{-7}	3.72×10^{-7}	2.28×10^{-7}	8.15×10^{-8}	1.47×10^{-2}	6.99×10^{-7}	4.18×10^{-7}	2.69×10^{-7}
$MgSiO_3$	3.43×10^{-6}	2.14×10^{-6}	1.28×10^{-6}	4.69×10^{-7}	9.30×10^{-4}	4.06×10^{-6}	2.38×10^{-6}	1.51×10^{-6}
Mg_2SiO_4	2.70×10^{-5}	1.68×10^{-5}	1.00×10^{-5}	3.71×10^{-6}	1.23×10^{-1}	3.21×10^{-5}	1.87×10^{-5}	1.19×10^{-5}
MgO	6.42×10^{-8}	4.08×10^{-8}	2.51×10^{-8}	8.78×10^{-9}	3.46×10^{-8}	7.67×10^{-8}	4.61×10^{-8}	2.95×10^{-8}
Al_2O_3	1.26×10^{-6}	7.80×10^{-7}	4.77×10^{-7}	1.70×10^{-2}	1.71×10^{-2}	1.47×10^{-6}	8.57×10^{-7}	5.59×10^{-7}
FeO	7.39×10^{-6}	5.01×10^{-6}	3.25×10^{-6}	1.23×10^{-6}	4.66×10^{-7}	8.64×10^{-6}	5.58×10^{-6}	3.76×10^{-6}
Fe_3O_4	1.05×10^{-4}	7.07×10^{-5}	4.52×10^{-5}	1.73×10^{-5}	7.01×10^{-6}	1.22×10^{-4}	7.84×10^{-5}	5.27×10^{-5}
Total	1.45×10^{-4}	9.69×10^{-5}	2.26×10^{-2}	6.18×10^{-2}	2.02×10^{-1}	1.83×10^{-4}	8.05×10^{-4}	2.14×10^{-2}
	M15bE0.82	M15bE0.89	M15bE0.92	M15bE1.69	M15bE2.63	M15bE10.7	M15cE2.06	M15cE1.94
C	3.87×10^{-3}	4.34×10^{-2}	4.31×10^{-2}	4.47×10^{-2}	4.48×10^{-2}	4.47×10^{-2}	4.47×10^{-2}	4.47×10^{-2}
SiC	3.37×10^{-12}	5.84×10^{-12}	6.10×10^{-12}	2.11×10^{-12}	3.56×10^{-10}	6.54×10^{-12}	1.13×10^{-12}	1.24×10^{-12}
TiC	1.28×10^{-12}	3.97×10^{-12}	4.89×10^{-12}	2.61×10^{-12}	1.96×10^{-12}	9.59×10^{-12}	1.17×10^{-12}	1.29×10^{-12}
Si	0	0	0	2.87×10^{-11}	7.98×10^{-8}	3.66×10^{-28}	6.31×10^{-10}	1.20×10^{-10}
SiO_2	3.12×10^{-7}	2.07×10^{-7}	2.00×10^{-7}	9.71×10^{-8}	5.74×10^{-8}	1.72×10^{-7}	7.36×10^{-8}	7.90×10^{-8}
$MgSiO_3$	1.75×10^{-6}	1.16×10^{-6}	1.12×10^{-6}	5.57×10^{-7}	5.54×10^{-4}	9.74×10^{-7}	1.83×10^{-6}	1.47×10^{-6}
Mg_2SiO_4	1.37×10^{-5}	9.17×10^{-6}	8.84×10^{-6}	4.82×10^{-6}	1.20×10^{-1}	7.65×10^{-6}	7.90×10^{-2}	6.43×10^{-2}
MgO	3.43×10^{-8}	2.29×10^{-8}	2.21×10^{-8}	1.05×10^{-8}	6.11×10^{-9}	1.89×10^{-8}	7.90×10^{-9}	8.49×10^{-9}
Al_2O_3	6.42×10^{-7}	4.36×10^{-7}	4.21×10^{-7}	1.89×10^{-2}	1.74×10^{-2}	1.57×10^{-4}	1.83×10^{-2}	1.84×10^{-2}
FeO	4.30×10^{-6}	2.99×10^{-6}	2.89×10^{-6}	1.46×10^{-6}	8.85×10^{-7}	2.51×10^{-6}	1.12×10^{-6}	1.20×10^{-6}
Fe_3O_4	6.02×10^{-5}	4.14×10^{-5}	3.99×10^{-5}	2.04×10^{-5}	1.25×10^{-5}	3.48×10^{-5}	1.58×10^{-5}	1.68×10^{-5}
Total	3.96×10^{-3}	4.34×10^{-2}	4.31×10^{-2}	6.37×10^{-2}	1.83×10^{-1}	4.49×10^{-2}	1.42×10^{-1}	1.27×10^{-1}
	M15cE1.90	M15cE1.86	M15cE2.24	M15cE2.60	M15cE3.43	M20aE0.53	M20aE0.65	M20aE0.81
C	4.47×10^{-2}	4.47×10^{-2}	4.47×10^{-2}	4.47×10^{-2}	4.48×10^{-2}	2.36×10^{-2}	2.37×10^{-2}	2.37×10^{-2}
SiC	1.26×10^{-12}	1.34×10^{-12}	1.21×10^{-12}	4.86×10^{-10}	3.61×10^{-10}	3.72×10^{-12}	5.40×10^{-12}	6.39×10^{-12}
TiC	1.32×10^{-12}	1.41×10^{-12}	1.06×10^{-12}	8.59×10^{-13}	6.09×10^{-13}	4.57×10^{-17}	6.76×10^{-13}	1.03×10^{-11}
Si	5.04×10^{-11}	1.40×10^{-11}	2.67×10^{-9}	1.40×10^{-8}	1.29×10^{-8}	0	0	0
SiO_2	8.09×10^{-8}	8.60×10^{-8}	6.66×10^{-8}	5.70×10^{-8}	1.11×10^{-2}	4.53×10^{-7}	3.84×10^{-7}	3.34×10^{-7}
$MgSiO_3$	1.08×10^{-6}	5.49×10^{-7}	1.46×10^{-4}	4.15×10^{-4}	7.02×10^{-4}	2.68×10^{-6}	2.35×10^{-6}	1.85×10^{-6}
Mg_2SiO_4	4.06×10^{-2}	1.41×10^{-3}	1.15×10^{-1}	1.28×10^{-1}	1.28×10^{-1}	2.11×10^{-5}	1.88×10^{-5}	1.47×10^{-5}
MgO	8.71×10^{-9}	9.27×10^{-9}	7.13×10^{-9}	6.03×10^{-9}	2.75×10^{-7}	4.88×10^{-8}	4.16×10^{-8}	3.42×10^{-8}
Al_2O_3	1.84×10^{-2}	1.84×10^{-2}	1.83×10^{-2}	1.82×10^{-2}	1.82×10^{-2}	1.00×10^{-6}	8.24×10^{-7}	1.83×10^{-3}
FeO	1.22×10^{-6}	1.30×10^{-6}	1.02×10^{-6}	8.61×10^{-7}	6.86×10^{-7}	5.91×10^{-6}	5.17×10^{-6}	4.36×10^{-6}
Fe_3O_4	1.72×10^{-5}	1.82×10^{-5}	1.43×10^{-5}	1.24×10^{-5}	1.04×10^{-5}	8.39×10^{-5}	7.28×10^{-5}	6.31×10^{-5}

Table 3 *continued on next page*

Table 3 *(continued)*

Dust Species	Models							
Total	1.03×10^{-1}	6.46×10^{-2}	1.78×10^{-1}	1.92×10^{-1}	2.03×10^{-1}	2.37×10^{-2}	2.38×10^{-2}	2.56×10^{-2}
	M20aE0.85	M20aE1.39	M20aE1.47	M20aE2.43	M20aE2.50	M20aE4.15	M20bE0.78	M20bE1.04
C	2.37×10^{-2}	2.37×10^{-2}	2.37×10^{-2}	2.37×10^{-2}	2.37×10^{-2}	2.38×10^{-2}	2.37×10^{-2}	2.37×10^{-2}
SiC	6.53×10^{-12}	6.17×10^{-12}	4.88×10^{-12}	3.55×10^{-12}	3.57×10^{-12}	2.60×10^{-12}	6.52×10^{-12}	6.19×10^{-12}
TiC	1.10×10^{-11}	1.41×10^{-11}	9.82×10^{-12}	8.09×10^{-12}	7.95×10^{-12}	5.89×10^{-12}	1.08×10^{-11}	1.36×10^{-11}
Si	0	1.34×10^{-15}	1.86×10^{-11}	5.35×10^{-7}	3.15×10^{-7}	2.85×10^{-7}	0	1.12×10^{-30}
SiO_2	3.18×10^{-7}	3.23×10^{-7}	3.20×10^{-7}	2.51×10^{-7}	2.47×10^{-7}	2.90×10^{-2}	3.34×10^{-7}	2.52×10^{-7}
$MgSiO_3$	1.75×10^{-6}	4.36×10^{-6}	4.14×10^{-6}	3.40×10^{-6}	3.48×10^{-6}	8.33×10^{-4}	1.94×10^{-6}	5.05×10^{-6}
Mg_2SiO_4	1.39×10^{-5}	4.06×10^{-2}	3.00×10^{-2}	6.10×10^{-2}	5.62×10^{-2}	8.59×10^{-2}	1.54×10^{-5}	4.28×10^{-3}
MgO	3.31×10^{-8}	1.96×10^{-7}	5.85×10^{-7}	6.71×10^{-7}	6.93×10^{-7}	8.43×10^{-7}	3.55×10^{-8}	2.78×10^{-8}
Al_2O_3	3.88×10^{-3}	1.85×10^{-2}	1.34×10^{-2}	1.15×10^{-2}	8.38×10^{-3}	9.92×10^{-3}	1.27×10^{-3}	7.87×10^{-3}
FeO	4.24×10^{-6}	2.63×10^{-6}	4.40×10^{-6}	3.31×10^{-6}	3.27×10^{-6}	2.37×10^{-6}	4.51×10^{-6}	3.60×10^{-6}
Fe_3O_4	6.02×10^{-5}	6.80×10^{-5}	6.75×10^{-5}	5.26×10^{-5}	5.24×10^{-5}	3.89×10^{-5}	6.49×10^{-5}	4.88×10^{-5}
Total	2.77×10^{-2}	8.30×10^{-2}	6.73×10^{-2}	9.64×10^{-2}	8.84×10^{-2}	1.49×10^{-1}	2.51×10^{-2}	3.59×10^{-2}
	M20bE1.19	M20bE1.52	M20bE2.60	M20bE4.33	M20cE0.75	M20cE0.84	M20cE1.00	M20cE1.65
C	2.37×10^{-2}	2.37×10^{-2}	2.37×10^{-2}	2.38×10^{-2}	2.37×10^{-2}	2.37×10^{-2}	2.37×10^{-2}	2.37×10^{-2}
SiC	5.75×10^{-12}	5.55×10^{-12}	3.28×10^{-12}	2.46×10^{-12}	6.45×10^{-12}	6.73×10^{-12}	5.41×10^{-12}	5.72×10^{-12}
TiC	1.24×10^{-11}	1.27×10^{-11}	7.34×10^{-12}	5.61×10^{-12}	9.94×10^{-12}	1.13×10^{-11}	1.07×10^{-11}	1.45×10^{-11}
Si	2.23×10^{-19}	2.46×10^{-13}	4.49×10^{-7}	2.64×10^{-7}	0	0	7.82×10^{-35}	3.11×10^{-9}
SiO_2	2.15×10^{-7}	3.14×10^{-7}	2.41×10^{-7}	1.81×10^{-2}	3.37×10^{-7}	3.24×10^{-7}	2.70×10^{-7}	3.02×10^{-7}
$MgSiO_3$	4.63×10^{-6}	4.11×10^{-6}	3.37×10^{-6}	1.02×10^{-3}	1.97×10^{-6}	1.78×10^{-6}	5.22×10^{-6}	3.92×10^{-6}
Mg_2SiO_4	1.47×10^{-2}	4.30×10^{-2}	6.13×10^{-2}	8.71×10^{-2}	1.57×10^{-5}	1.41×10^{-5}	4.44×10^{-3}	5.35×10^{-2}
MgO	2.36×10^{-8}	6.02×10^{-7}	6.99×10^{-7}	8.22×10^{-7}	3.60×10^{-8}	3.33×10^{-8}	2.98×10^{-8}	6.08×10^{-7}
Al_2O_3	1.14×10^{-2}	1.80×10^{-2}	1.09×10^{-2}	8.66×10^{-3}	5.62×10^{-4}	3.46×10^{-3}	9.61×10^{-3}	1.92×10^{-2}
FeO	3.11×10^{-6}	4.33×10^{-6}	3.18×10^{-6}	2.27×10^{-6}	4.56×10^{-6}	4.26×10^{-6}	3.81×10^{-6}	4.14×10^{-6}
Fe_3O_4	4.25×10^{-5}	6.67×10^{-5}	5.08×10^{-5}	3.72×10^{-5}	6.56×10^{-5}	6.12×10^{-5}	5.16×10^{-5}	6.40×10^{-5}
Total	4.99×10^{-2}	8.49×10^{-2}	9.62×10^{-2}	1.38×10^{-1}	2.43×10^{-2}	2.72×10^{-2}	3.78×10^{-2}	9.66×10^{-2}
	M20cE2.76	M20cE2.85	M20cE5.03	M20cE8.86	M20dE4.3	M20dE5.9	M20dE18.1	M20dE64.5
C	2.37×10^{-2}	2.37×10^{-2}	2.38×10^{-2}	2.42×10^{-2}	1.47×10^{-2}	2.30×10^{-2}	2.37×10^{-2}	2.36×10^{-2}
SiC	3.30×10^{-12}	3.30×10^{-12}	9.78×10^{-11}	3.02×10^{-10}	5.73×10^{-13}	2.50×10^{-13}	3.16×10^{-13}	7.28×10^{-14}
TiC	7.45×10^{-12}	6.80×10^{-12}	4.97×10^{-12}	3.49×10^{-12}	1.59×10^{-12}	6.30×10^{-13}	5.01×10^{-13}	1.47×10^{-13}
Si	4.72×10^{-7}	4.29×10^{-7}	2.02×10^{-7}	5.47×10^{-4}	3.11×10^{-12}	4.39×10^{-11}	5.86×10^{-9}	3.58×10^{-9}
SiO_2	2.33×10^{-7}	7.95×10^{-7}	2.50×10^{-2}	3.21×10^{-3}	1.02×10^{-1}	9.35×10^{-8}	1.64×10^{-7}	1.45×10^{-7}
$MgSiO_3$	2.41×10^{-5}	2.32×10^{-5}	1.02×10^{-3}	6.83×10^{-3}	2.41×10^{-5}	3.64×10^{-6}	2.53×10^{-6}	2.22×10^{-6}
Mg_2SiO_4	6.89×10^{-2}	6.86×10^{-2}	8.70×10^{-2}	8.76×10^{-2}	6.44×10^{-2}	4.64×10^{-2}	2.11×10^{-2}	1.22×10^{-2}
MgO	6.59×10^{-7}	7.35×10^{-7}	7.60×10^{-7}	2.02×10^{-6}	1.73×10^{-6}	5.26×10^{-6}	6.62×10^{-7}	5.76×10^{-7}
Al_2O_3	1.19×10^{-2}	1.09×10^{-2}	8.58×10^{-3}	3.63×10^{-3}	2.64×10^{-3}	7.47×10^{-3}	5.58×10^{-3}	2.46×10^{-3}
FeO	3.05×10^{-6}	3.05×10^{-6}	2.01×10^{-6}	1.36×10^{-6}	7.79×10^{-7}	1.49×10^{-6}	2.08×10^{-6}	1.72×10^{-6}
Fe_3O_4	4.88×10^{-5}	4.90×10^{-5}	3.31×10^{-5}	2.32×10^{-5}	1.42×10^{-5}	2.78×10^{-5}	3.57×10^{-5}	2.95×10^{-5}
Total	1.04×10^{-1}	1.03×10^{-1}	1.45×10^{-1}	1.31×10^{-1}	1.84×10^{-1}	7.70×10^{-2}	5.05×10^{-2}	3.84×10^{-2}
	M20E78.9	M20dE88.4	M20dE124.0	M25aE0.99	M25aE1.57	M25aE4.73	M25aE6.17	M25aE7.42

Table 3 *continued on next page*

Table 3 *(continued)*

Dust Species	Models							
C	2.00×10^{-2}	1.44×10^{-2}	1.12×10^{-2}	1.37×10^{-2}	1.37×10^{-2}	1.38×10^{-2}	1.39×10^{-2}	1.39×10^{-2}
SiC	1.48×10^{-12}	3.84×10^{-13}	4.61×10^{-14}	7.82×10^{-13}	4.63×10^{-13}	2.09×10^{-13}	1.56×10^{-13}	1.37×10^{-13}
TiC	4.62×10^{-13}	1.08×10^{-12}	1.00×10^{-13}	1.96×10^{-12}	1.15×10^{-12}	7.05×10^{-13}	4.86×10^{-13}	4.67×10^{-13}
Si	8.61×10^{-9}	2.68×10^{-12}	2.26×10^{-15}	4.86×10^{-6}	7.67×10^{-7}	1.34×10^{-1}	1.16×10^{-1}	1.22×10^{-1}
SiO_2	1.51×10^{-4}	1.24×10^{-4}	1.20×10^{-2}	5.92×10^{-8}	4.26×10^{-8}	4.19×10^{-2}	5.43×10^{-2}	4.59×10^{-2}
$MgSiO_3$	3.18×10^{-6}	8.09×10^{-5}	2.18×10^{-5}	7.67×10^{-7}	1.11×10^{-6}	1.13×10^{-3}	2.26×10^{-3}	3.05×10^{-3}
Mg_2SiO_4	1.54×10^{-2}	4.50×10^{-2}	1.69×10^{-3}	3.59×10^{-2}	6.15×10^{-2}	1.60×10^{-1}	2.62×10^{-1}	2.77×10^{-1}
MgO	4.21×10^{-2}	2.48×10^{-3}	7.47×10^{-6}	1.20×10^{-7}	8.15×10^{-8}	8.00×10^{-8}	5.18×10^{-7}	7.36×10^{-6}
Al_2O_3	4.93×10^{-3}	4.37×10^{-3}	7.11×10^{-5}	9.32×10^{-3}	1.42×10^{-2}	1.91×10^{-2}	2.41×10^{-2}	1.97×10^{-2}
FeO	3.76×10^{-5}	1.06×10^{-6}	3.72×10^{-7}	7.86×10^{-7}	5.55×10^{-7}	1.01×10^{-6}	8.11×10^{-7}	9.69×10^{-7}
Fe_3O_4	1.51×10^{-3}	1.55×10^{-5}	7.91×10^{-6}	1.16×10^{-5}	8.30×10^{-6}	1.49×10^{-5}	1.31×10^{-5}	1.80×10^{-5}
Total	8.45×10^{-2}	6.65×10^{-2}	2.51×10^{-2}	5.90×10^{-2}	8.95×10^{-2}	4.76×10^{-1}	5.21×10^{-1}	5.31×10^{-1}
	M25aE14.8	M25bE8.40	M25bE9.73	M25bE18.4	M25d3E0.89	M25d3E0.92	M25d3E1.04	M25d3E1.20
C	1.48×10^{-2}	1.39×10^{-2}	1.39×10^{-2}	1.40×10^{-2}	1.37×10^{-2}	1.37×10^{-2}	3.60×10^{-3}	1.98×10^{-3}
SiC	1.13×10^{-13}	1.71×10^{-13}	1.93×10^{-13}	5.79×10^{-14}	4.97×10^{-13}	9.73×10^{-11}	8.99×10^{-10}	1.63×10^{-9}
TiC	4.99×10^{-13}	6.13×10^{-13}	6.77×10^{-13}	1.65×10^{-13}	1.30×10^{-12}	5.97×10^{-13}	3.99×10^{-12}	1.36×10^{-12}
Si	1.78×10^{-1}	3.43×10^{-5}	8.73×10^{-4}	5.31×10^{-5}	3.58×10^{-6}	1.20×10^{-1}	1.20×10^{-1}	1.17×10^{-1}
SiO_2	9.06×10^{-2}	8.47×10^{-2}	1.11×10^{-1}	2.12×10^{-2}	5.93×10^{-8}	2.34×10^{-1}	5.57×10^{-2}	2.82×10^{-2}
$MgSiO_3$	7.19×10^{-3}	3.91×10^{-2}	1.10×10^{-3}	2.60×10^{-3}	7.11×10^{-7}	1.50×10^{-3}	2.27×10^{-2}	1.23×10^{-3}
Mg_2SiO_4	8.90×10^{-2}	2.46×10^{-1}	2.56×10^{-1}	1.03×10^{-1}	3.68×10^{-2}	2.08×10^{-1}	1.73×10^{-1}	2.57×10^{-2}
MgO	1.35×10^{-4}	8.59×10^{-6}	3.89×10^{-10}	7.67×10^{-5}	1.07×10^{-7}	5.08×10^{-8}	3.27×10^{-5}	8.42×10^{-5}
Al_2O_3	2.30×10^{-3}	6.48×10^{-3}	5.29×10^{-2}	1.62×10^{-3}	9.70×10^{-3}	4.82×10^{-2}	2.51×10^{-3}	9.10×10^{-4}
FeO	1.43×10^{-6}	3.11×10^{-7}	1.70×10^{-7}	1.12×10^{-6}	7.91×10^{-7}	2.17×10^{-6}	8.58×10^{-7}	1.24×10^{-6}
Fe_3O_4	3.05×10^{-5}	5.68×10^{-6}	3.81×10^{-6}	2.22×10^{-5}	1.16×10^{-5}	4.03×10^{-5}	1.76×10^{-5}	2.65×10^{-5}
Total	3.88×10^{-1}	3.91×10^{-1}	4.36×10^{-1}	1.43×10^{-1}	6.03×10^{-2}	6.93×10^{-1}	5.38×10^{-1}	5.31×10^{-1}
	M25d2E2.53	M25d2E2.64	M25d2E2.78	M25d2E3.07	M25d1E3.30	M25d1E4.72	M25d1E7.08	
C	1.37×10^{-2}	1.37×10^{-2}	1.37×10^{-2}	4.44×10^{-3}	1.37×10^{-2}	1.37×10^{-2}	1.37×10^{-2}	
SiC	1.54×10^{-12}	1.28×10^{-12}	8.54×10^{-13}	7.19×10^{-11}	6.65×10^{-13}	4.26×10^{-13}	1.74×10^{-11}	
TiC	5.57×10^{-12}	4.11×10^{-12}	2.12×10^{-12}	3.34×10^{-12}	1.70×10^{-12}	1.29×10^{-12}	6.07×10^{-13}	
Si	8.12×10^{-3}	7.20×10^{-2}	7.20×10^{-2}	1.39×10^{-1}	7.88×10^{-2}	7.29×10^{-2}	7.26×10^{-2}	
SiO_2	3.05×10^{-1}	3.29×10^{-1}	1.85×10^{-1}	5.76×10^{-2}	1.26×10^{-1}	3.40×10^{-1}	3.38×10^{-1}	
$MgSiO_3$	5.58×10^{-4}	1.07×10^{-4}	2.62×10^{-3}	1.07×10^{-3}	1.96×10^{-3}	5.35×10^{-5}	6.67×10^{-5}	
Mg_2SiO_4	2.53×10^{-1}	2.52×10^{-1}	2.52×10^{-1}	1.98×10^{-2}	2.52×10^{-1}	2.52×10^{-1}	2.52×10^{-1}	
MgO	2.13×10^{-7}	5.97×10^{-8}	1.43×10^{-9}	6.74×10^{-5}	1.45×10^{-9}	9.97×10^{-10}	7.16×10^{-3}	
Al_2O_3	4.28×10^{-2}	4.42×10^{-2}	4.78×10^{-2}	7.86×10^{-4}	5.58×10^{-2}	5.70×10^{-2}	5.70×10^{-2}	
FeO	1.20×10^{-5}	8.67×10^{-6}	2.11×10^{-6}	1.38×10^{-6}	7.25×10^{-7}	9.78×10^{-6}	1.02×10^{-5}	
Fe_3O_4	5.68×10^{-4}	7.39×10^{-4}	3.91×10^{-5}	2.90×10^{-5}	1.23×10^{-5}	1.07×10^{-3}	1.72×10^{-3}	
Total	6.26×10^{-1}	7.35×10^{-1}	5.89×10^{-1}	3.05×10^{-1}	5.31×10^{-1}	7.40×10^{-1}	7.68×10^{-1}	

NOTE—The single element Fe-group grain species are excluded from this table due to very inconsistent non-negligible yields. Entries with a dash line indicate negligible and effectively zero amounts of that species being produced for the given model.

REFERENCES

Akima, H. 1970, Journal of the ACM (JACM), 17, 589

Andrews, S., Fryer, C., Even, W., Jones, S., & Pignatari, M. 2020, ApJ, 890, 35, doi: 10.3847/1538-4357/ab64f8

Biscaro, C., & Cherchneff, I. 2016, A&A, 589, A132, doi: 10.1051/0004-6361/201527769

Brooker, E. S., Stangl, S. M., Mauney, C. M., & Fryer, C. L. 2021, Dependence of Dust Formation on the Supernova Explosion. https://arxiv.org/abs/2103.12781

Castor, J. I., Abbott, D. C., & Klein, R. I. 1975, ApJ, 195, 157, doi: 10.1086/153315

Fryer, C., Benz, W., Herant, M., & Colgate, S. A. 1999, ApJ, 516, 892, doi: 10.1086/307119

Fryer, C. L., Andrews, S., Even, W., Heger, A., & Safi-Harb, S. 2018, ApJ, 856, 63, doi: 10.3847/1538-4357/aaaf6f

Harris, C. R., Millman, K. J., van der Walt, S. J., et al. 2020, Nature, 585, 357–362, doi: 10.1038/s41586-020-2649-2

Herant, M., Benz, W., Hix, W. R., Fryer, C. L., & Colgate, S. A. 1994, ApJ, 435, 339, doi: 10.1086/174817

Hindmarsh, A. C. 1983, Scientific computing, 55

Kozasa, T., & Hasegawa, H. 1987, Progress of Theoretical Physics, 77, 1402–1410

Lam, S. K., Pitrou, A., & Seibert, S. 2015, in Proceedings of the Second Workshop on the LLVM Compiler Infrastructure in HPC, LLVM '15 (New York, NY, USA: Association for Computing Machinery), doi: 10.1145/2833157.2833162

McBride, B. J. 1993, Coefficients for calculating thermodynamic and transport properties of individual species, Vol. 4513 (NASA Langley Research Center)

Nozawa, T., & Kozasa, T. 2013, The Astrophysical Journal, 776, 24, doi: 10.1088/0004-637x/776/1/24

Nozawa, T., Kozasa, T., & Habe, A. 2006, The Astrophysical Journal, 648, 435, doi: 10.1086/505639

Nozawa, T., Kozasa, T., Umeda, H., Maeda, K., & Nomoto, K. 2003, The Astrophysical Journal, 598, 785, doi: 10.1086/379011

Sluder, A., Milosavljević, M., & Montgomery, M. H. 2018, Monthly Notices of the Royal Astronomical Society, 480, 5580, doi: 10.1093/mnras/sty2060

Villata, M. 1992, Astronomy and Astrophysics, 257, 677

Virtanen, P., Gommers, R., Oliphant, T. E., et al. 2020, Nature Methods, 17, 261, doi: 10.1038/s41592-019-0686-2